INORGANIC CHEMISTRY FRONTIERS

RESEARCH ARTICLE

View Article Online
View Journal | View Issue

Cite this: *Inorg. Chem. Front.*, 2021, **8**, 1303

Two novel nickel cluster substituted polyoxometalates: syntheses, structures and their photocatalytic activities, magnetic behaviors, and proton conduction properties†

Yi Chen,[a] Zheng-Wei Guo,[a] Ya-Peng Chen,[b] Zan-Yong Zhuang,[b] Guo-Qiang Wang,[b] Xin-Xiong Li,*[a] Shou-Tian Zheng*[a] and Guo-Yu Yang*[c]

Received 30th November 2020,
Accepted 6th January 2021

DOI: 10.1039/d0qi01410a

rsc.li/frontiers-inorganic

Two novel nickel cluster substituted polyoxometalates (POMs), $H_7Na_{19}(H_2O)_{26}\{Ni_{12}(OH)_9(PO_4)_4(A\text{-}\alpha\text{-}SiW_9O_{34})[W_4O_{10}(OH)(PO_2(OH)_2)_2(A\text{-}\alpha\text{-}SiW_9O_{34})_2]\}\cdot 4C_2H_8N\cdot 27H_2O$ (**1**) and $H_{26.5}K_{2.5}Na(H_2O)_{16}[Ni_6(OH)(BO_3)_2(dien)_2(B\text{-}\alpha\text{-}SiW_{10}O_{37})_2]_2\cdot 24H_2O$ (**2**) (dien = diethylenetriamine), have been successfully prepared. **1** is a Ni_{12}-substituted POM comprised of a novel $\{Ni_{12}(OH)_9(PO_4)_4\}$ core, an A-α-$\{SiW_9O_{34}\}$ unit and an uncommon $\{W_4O_{10}(OH)[PO_2(OH)_2]_2(A\text{-}\alpha\text{-}SiW_9O_{34})_2\}$ fragment. **2** is a Ni_6-substituted sandwich-type POM constructed from two B-α-$\{SiW_{10}O_{37}\}$ units and an unusual boat-like $\{Ni_6(OH)(BO_3)_2(dien)_2\}$ cluster. Photocatalytic study reveals that **2** shows a moderate catalytic activity in visible-light-driven CO_2 reduction reactions. Additionally, the magnetic behaviors and the proton conduction performances of the compounds were investigated.

1. Introduction

Polyoxometalates (POMs), as early-transition-metal oxide clusters, have been attracting considerable interest due to their intriguing structural diversity and potential applications in magnetism, electronics, photoluminescence, medicine, catalysis, ion exchange, and photochemistry.[1–11] The saturated Keggin-/Dawson-type POM clusters can often be transformed into a variety of metastable lacunary species with different vacancies by the loss of one or more MO_6 polyhedra under specific conditions.[12] These lacunary polyanions are highly active to all kinds of transition metal (TM) ions, and can serve as good multidentate oxo ligands to induce TM ions to form high-nuclear clusters, giving rise to a class of TM-substituted POMs (TMSPs) with interesting physicochemical properties.[13–16] For instance, TMSPs are ideal materials used to investigate the interactions between TM ions within clusters. Among various TMSPs, the nickel-containing TMSPs are particularly interesting and have been extensively studied by virtue of their fascinating structural diversity and unique magnetic/catalytic nature.[17–21] For example, nickel-based TMSPs are a class of significant single-molecule magnetism candidates[22–24] and photocatalysts.[25–29] So far, a number of nickel-containing TMSPs have been studied (Table S1, ESI†). However, most of them consist of small nickel clusters with no more than six Ni^{2+} ions, and the number of TMSPs containing larger nickel clusters with more than six Ni^{2+} ions is still relatively limited. High-nuclear nickel clusters are usually richer in configuration, which may result in unexpected electronic/magnetic/catalytic performances. Hence, the exploration of novel TMSPs which incorporate larger nickel clusters is of great significance to the further development of POM chemistry.

Our group has been devoted to the study of nickel cluster incorporated TMSPs, and reported a series of interesting structures in recent years.[23,30–36] As part of our continuous work in this area, we have successfully prepared another two TMSPs incorporating/containing different large nickel clusters: $H_7Na_{19}(H_2O)_{26}\{Ni_{12}(OH)_9(PO_4)_4(A\text{-}\alpha\text{-}SiW_9O_{34})[W_4O_{10}(OH)(PO_2(OH)_2)_2(A\text{-}\alpha\text{-}SiW_9O_{34})_2]\}\cdot 4C_2H_8N\cdot 27H_2O$ (**1**) and $H_{26.5}K_{2.5}Na(H_2O)_{16}[Ni_6(OH)(BO_3)_2(dien)_2(B\text{-}\alpha\text{-}SiW_{10}O_{37})_2]_2\cdot 24H_2O$ (**2**). As far as we know, **1** is a brand new nickel-based TMSP in which a twelve-nuclear nickel cluster was stabilized by an A-α-$\{SiW_9O_{34}\}$ unit and an unprecedented $\{W_4O_{10}(OH)[PO_2(OH)_2]_2(A\text{-}\alpha\text{-}SiW_9O_{34})_2\}$ fragment. **2** is an impor-

[a]*College of Chemistry, Fuzhou University, Fuzhou, Fujian 350108, People's Republic of China. E-mail: lxx@fzu.edu.cn, stzheng@fzu.edu.cn*
[b]*Key Laboratory of Advanced Materials Technologies, College of Materials Science and Engineering, Fuzhou University, Fuzhou, Fujian 350108, People's Republic of China*
[c]*MOE Key Laboratory of Cluster Science, School of Chemistry and Chemical Engineering, Beijing Institute of Technology, Beijing, 100081, China. E-mail: ygy@bit.edu.cn*

†Electronic supplementary information (ESI) available: Additional figures and tables. CCDC 1585405 and 2043277. For ESI and crystallographic data in CIF or other electronic format see DOI: 10.1039/d0qi01410a

tant new member of hexa-nuclear nickel cluster substituted TMSP, in which an unusual boat-like $\{Ni_6(OH)(BO_3)_2(dien)_2\}$ cluster was observed for the first time. In both compounds, interesting *in situ* structural transformations based on the $\{A\text{-}\alpha\text{-}SiW_9O_{34}\}$ unit were observed. Additionally, the photocatalytic activity, magnetic behaviors, and the proton conduction performance of the compounds were initially evaluated.

2. Experimental section

2.1 Materials and instruments

All chemical reagents were purchased and directly used without purification. $Na_{10}[A\text{-}\alpha\text{-}SiW_9O_{34}]\cdot 18H_2O$ was synthesized according to the literature method.[37] IR spectra were recorded on an Opus Vertex 70 FT-IR infrared spectrophotometer in the range of 4000–500 cm^{-1}. Inductively coupled plasma atomic emission spectrometry (ICP-AES) was performed on an Ultima2 spectrometer. Elemental analyses of C, H, and N were conducted on a Vario EL III elemental analyzer. Powder X-ray diffraction (PXRD) patterns were collected on a Philips X'Pert-MPD diffractometer with CuK_α radiation (λ = 1.54056 Å). Thermogravimetric analysis was conducted on a Mettler Toledo TGA/SDTA 851^e analyzer under an air-flow atmosphere with a 10 °C min^{-1} heating rate in the temperature of 30–800 °C. UV-vis diffuse reflection spectra were collected using a PerkinElmer Lambda 35 spectrophotometer. Magnetic properties analyses (Variable temperature susceptibility measurements) were carried out on monocrystalline samples with a Quantum Design PPMS-9T magnetometer within the temperature range of 1.99–300 K in a magnetic field of 0.1 T. The experimental susceptibilities were corrected for Pascal's constants.

2.2 Syntheses

Synthesis of $H_7Na_{19}(H_2O)_{26}\{Ni_{12}(OH)_9(PO_4)_4(A\text{-}\alpha\text{-}SiW_9O_{34})[W_4O_{10}(OH)(PO_2(OH)_2)_2(A\text{-}\alpha\text{-}SiW_9O_{34})_2]\}\cdot 4C_2H_8N\cdot 27H_2O$ (1). $Na_{10}[A\text{-}\alpha\text{-}SiW_9O_{34}]\cdot 18H_2O$ (0.423 g, 0.16 mmol), $NiCl_2\cdot 6H_2O$ (0.070 g, 0.29 mmol) and dimethylamine hydrochloride (0.200 g, 2.45 mmol) were dissolved in 5 mL 1 mol L^{-1} NaH_2PO_4 (aq). After one hour of stirring, the pH value of the resulting solution was adjusted to 9 by 3 mol L^{-1} NaOH (2 mL). And then the mixture was sealed in a glass vial (20 mL) and heated at 100 °C for 96 h. The pH value after reaction was 7. After the reaction was cooled to room temperature, green block crystals were obtained. The phase purity of **1** was confirmed by PXRD (Fig. S1, ESI†). Yield: 17.14% based on $NiCl_2\cdot 6H_2O$. Elemental analysis calcd (found %) for **1**: C, 0.90 (0.81); H, 1.51 (1.53); N, 0.52 (0.46). ICP analyses (based on dried sample) calcd (found %) for **1**: Na, 4.11 (3.83); Si, 0.79 (0.69); P, 1.75 (1.33); Ni, 6.64 (6.46); W, 53.73 (53.19). IR (solid ATR, ν/cm^{-1}): 3373(m), 2109(w), 1628(vs), 1465(vs), 1098(w), 1042(w), 983(s), 935(m), 850(w), 806(m), 675(w), 621(w), 502(m) (Fig. S2, ESI†).

Synthesis of $H_{26.5}K_{2.5}Na(H_2O)_{16}[Ni_6(OH)(BO_3)_2(dien)_2(B\text{-}\alpha\text{-}SiW_{10}O_{37})_2]_2\cdot 24H_2O$ (2). $Na_{10}[A\text{-}\alpha\text{-}SiW_9O_{34}]\cdot 18H_2O$ (0.352 g, 0.120 mmol), $Ni(Ac)_2\cdot 4H_2O$ (0.102 g, 0.410 mmol), $Gd(NO_3)_3\cdot 6H_2O$ (0.087 g, 0.193 mmol), $Li_2B_4O_7$ (0.085 g, 0.503 mmol) and $K_2B_{10}O_{16}\cdot 8H_2O$ (0.070 g, 0.119 mmol) were dissolved in 4 mL H_2O. And then, 0.02 mL of dien was added. After one hour of stirring, the resulting mixture was sealed in a glass vial (20 mL) and heated at 80 °C for 6 days. The pH values before and after reaction were 7 and 7, respectively. After the reaction was cooled to room temperature, the filtrate was left to evaporate slowly at room temperature. Green block crystals were obtained three weeks later. The phase purity of **2** was confirmed by PXRD (Fig. S3, ESI†). Yield: 11.82% based on $Ni(Ac)_2\cdot 4H_2O$. Elemental analysis calcd (found %) for **2**: C, 1.58 (1.34); H, 1.33 (1.23); N, 1.39 (1.31). ICP analyses (based on dried sample) calcd (found %) for **2**: B, 0.35 (0.21); K, 0.80 (0.91); Na, 0.19 (0.22); Si, 0.92 (0.84); Ni, 5.82 (5.69); W, 60.83 (60.28). IR (solid ATR, ν/cm^{-1}): 3327(m), 1634(vs), 1345(vs), 1128(w) 1076(w), 985(s), 937(m), 871(w), 766(m), 658(w), 459(s) (Fig. S4, ESI†).

2.3 X-Ray crystallographic analysis

Single-crystal X-ray diffraction data for **1** and **2** was collected on a Bruker APEX II diffractometer at 175 K equipped with a fine focus, 2.0 kW sealed tube X-ray source (MoK_α radiation, λ = 0.71073 Å) operating at 50 kV and 30 mA. The program SADABS was used for absorption correction. The structures were solved by the direct method and refined on F^2 by full-matrix least-squares methods using the SHELX-2013 program package. All hydrogen atoms attached to carbon atoms were generated geometrically. The residual electron density that could not be sensibly modeled as solvents or anions were removed *via* the application of the SQUEEZE function in PLATON. The final formulas of **1** and **2** were determined by the combination of single-crystal X-ray diffractions with the elemental analyses, the thermogravimetric analyses, and charge balance. Crystallographic data for the structures reported in this work have been deposited in the Cambridge Crystallographic Data Center with CCDC 1585405, 2043277† for **1**, **2** respectively. Crystallographic data and structure refinements for **1** and **2** are summarized in Table 1.

3. Results and discussion

3.1 Crystal structure of $H_7Na_{19}(H_2O)_{26}\{Ni_{12}(OH)_9(PO_4)_4(A\text{-}\alpha\text{-}SiW_9O_{34})[W_4O_{10}(OH)(PO_2(OH)_2)_2(A\text{-}\alpha\text{-}SiW_9O_{34})_2]\}\cdot 4C_2H_8N\cdot 27H_2O$ (1)

Single crystal X-ray diffraction analysis indicates that compound **1** crystallizes in the monoclinic $P2_1/m$ space group. As shown in Fig. 1a, the polyanion of **1** consists of a trilacunary Keggin-type A-α-$\{SiW_9O_{34}\}$ ($\{A\text{-}SiW_9\}$) (Fig. 1b) unit, an unprecedented $\{W_4O_{10}(OH)[PO_2(OH)_2]_2(A\text{-}\alpha\text{-}SiW_9O_{34})_2\}$ ($\{A\text{-}P_2Si_2W_{22}\}$) (Fig. 1c) fragment and a central $\{Ni_{12}(OH)_9(PO_4)_4\}$ ($\{Ni_{12}\}$, Fig. 1d) core. The $\{A\text{-}P_2Si_2W_{22}\}$ fragment comes from an *in situ* structural transformation from the starting $\{A\text{-}SiW_9\}$ units and plays an important role in the construction of **1**. The $\{A\text{-}P_2Si_2W_{22}\}$ moiety is composed of two $\{A\text{-}SiW_9\}$ units bridged by an additional belt-

Table 1 Crystal data and structure refinements for compounds **1–2**

Compound	**1**	**2**
Empirical formula	$H_{159}C_8N_4Na_{19}Ni_{12}O_{199}P_6Si_3W_{31}$	$H_{160.5}B_4C_{16}N_{12}O_{202}K_{2.5}NaNi_{12}W_{40}$
M_r (g mol^{-1})	10 047.14	11 650.91
Temperature/K	175(2)	175(2)
Crystal system	Monoclinic	Trigonal
Space group	$P2_1/m$	$P3_221$
a (Å)	20.4528(8)	35.1946(18)
b (Å)	24.8351(9)	35.1946(18)
c (Å)	24.7637(9)	49.109(3)
α (°)	90.00	90
β (°)	113.0150(10)	90
γ (°)	90.00	120
V/Å^3	11 577.4(8)	52 680(6)
Z	2	6
ρ_{calcd} (g cm^{-3})	2.882	2.204
μ mm^{-1}	16.460	13.772
F(000)	8910	30 674
Crystal size/mm^3	0.2 × 0.15 × 0.2	0.2 × 0.12 × 0.2
Theta range/°	1.843 to 25.059	1.336 to 25.073
R_{int}	0.0260	0.0944
GooF	1.043	1.051
R [$I > 2\sigma$]	R_1 = 0.0246	R_1 = 0.0579
	wR_2 = 0.0601	wR_2 = 0.1275
R(all data)	R_1 = 0.0277	R_1 = 0.0749
	wR_2 = 0.0613	wR_2 = 0.1352

$R_1 = \sum(|F_o| - |F_c|)/\sum|F_o|$, $wR_2 = \{\sum[w(F_o^2 - F_c^2)^2]/\sum[w(F_o^2)^2]\}^{1/2}$.

like $\{W_4O_{10}(OH)[PO_2(OH)_2]_2\}$ ($\{P_2W_4\}$) (Fig. 1e) unit, which has never been found before. The $\{P_2W_4\}$ unit can be viewed as a $\{W_4O_{10}(OH)\}$ subunit consisting of four corner-sharing $\{WO_6\}$ octahedra further decorated by two $\{PO_4\}$ tetrahedra in the gaps at both ends. These additional $\{WO_6\}$ octahedra should be generated from *in situ* degradation of the starting $\{A\text{-}SiW_9\}$ units under the basic condition. So far, isopolyoxotungstate fragments based on a number of $\{WO_6\}$ octahedra which serve as a linker to construct novel multilacunary POM fragments are still rare. A representative example is a $\{Sb_2W_{20}O_{73}\}$ fragment comprised of two $\{SbW_9O_{34}\}$ units and an isopolytungstate fragment based on two $\{WO_6\}$ octahedra.[38] Therefore, the $\{A\text{-}P_2Si_2W_{22}\}$ subunit can be considered as an interesting multi-dentate oxo ligand to incorporate with the $\{Ni_{12}\}$ cluster. The central $\{Ni_{12}\}$ (Fig. 1f) cluster can be described as three tetrahedral $\{Ni_4(OH)_3\}$ (Fig. 1g) building blocks connected by a μ_3-$\{PO_4\}$ tetrahedron and three μ_4-$\{PO_4\}$ tetrahedra. In other words, the whole polyanion of **1** can also be understood as a $\{Ni_3(PO_4)_4\}$ core enveloped by three $\{(NiOH)_3(A\text{-}\alpha\text{-}SiW_9O_{34})\}$ units, in which the $\{Ni_3(PO_4)_4\}$ core displays a $\{Ni_3O_4\}$ (Fig. 1h) quasi-cubane structure, and an extra $\{P_2W_4\}$ cluster further anchors two trilacunary subunits. All the nickel ions in the $\{Ni_{12}\}$ cluster display a distorted octahedral coordination geometry, and the Ni–O bond lengths are in the range of 1.947(19)–2.230(18) Å. Bond valence sum (BVS) calculations manifest that all the nickel ions are in the +2 oxidation state and partial O atoms are in the -1 valence state (Tables S2–S4, ESI†). It is noteworthy that such a $\{Ni_{12}\}$ cluster is different from those reported nickel clusters containing twelve nickel ions in reported compounds including $[Ni_{12}(OH)_9WO_4(W_7O_{26}(OH))(PW_9O_{34})_3]^{25-}$,[39] $[Ni_{12}(OH)_9(CO_3)_3(PO_4)(SiW_9O_{34})_3]^{24-}$,[25] and $[(BO_3)_3PO_4Ni_{12}O_9(SiW_9O_{34})_3]^{36-}$.[40] The $\{Ni_{12}\}$ cluster in **1** was stabilized by four $\{PO_4\}$ tetrahedra besides the POM units, while the nickel clusters in reported examples were decorated by $\{WO_4\}$ tetrahedra or $\{CO_3/BO_3\}$ triangles mixed $\{PO_4\}$ with tetrahedra.

3.2 Crystal structure of $H_{26.5}K_{2.5}Na(H_2O)_{16}[Ni_6(OH)(BO_3)_2(dien)_2(B\text{-}\alpha\text{-}SiW_{10}O_{37})_2]_2{\cdot}24H_2O$ (2)

Single crystal X-ray diffraction analysis reveals that **2** crystallizes in the trigonal $P3_221$ chiral space group. The asymmetric unit of **2** contains two identical Ni_6-substituted polyanions (Fig. 2a and b), each of which is composed of two dilacunary B-α-$\{SiW_{10}O_{37}\}$ ($\{B\text{-}SiW_{10}\}$) units and a hexa-nuclear nickel cluster $\{Ni_6(OH)(BO_3)_2(dien)_2\}$ ($\{Ni_6\}$, Fig. 2c). The $\{B\text{-}SiW_{10}\}$ (Fig. 2d) comes from *in situ* structural transformation from the starting $\{A\text{-}SiW_9\}$ units. The central Ni_6 cluster can be regarded as a boat-like structure consisting of six nickel ions and is further stabilized by two dien ligands (Fig. 2e) and two $\{BO_3\}$ units (Fig. 2f). The four Ni atoms situated at the bottom of the boat are coordinated by five O atoms and one OH group. The other two Ni atoms at the bow and stern of the boat are coordinated by three N atoms from a dien ligand and three O atoms, respectively (Fig. 2g). All the nickel atoms in this $\{Ni_6\}$ cluster adopt a distorted octahedral coordination geometry with the Ni–O bond lengths in the range of 1.956(19)–2.332 (18) Å and the Ni-N bond lengths in the ranges of 2.022–2.100 Å. The BO_3 units is from the depolymerization of the starting $Li_2B_4O_7$ and $K_2B_{10}O_{16}{\cdot}8H_2O$, and the B–O bond lengths of the $\{BO_3\}$ segment are in the range of 1.313–1.438 Å. Up to now, the boron species have been seldom found in POM chemistry,[39] and such a $\{Ni_6\}$ cluster decorated by two $\{BO_3\}$ units has not been found before. BVS calculations manifested that all the nickel ions are in the +2 oxidation state and partial O

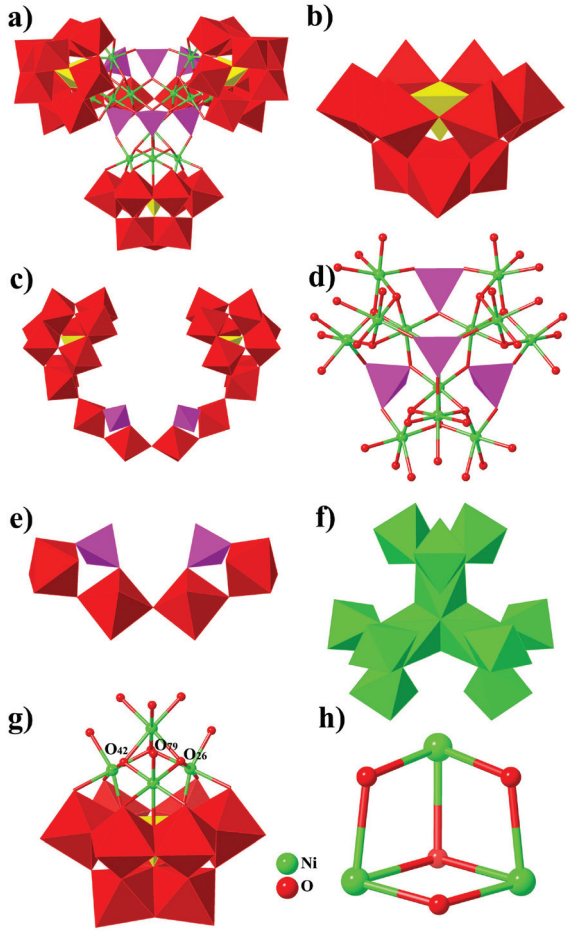

Fig. 1 (a) Combined polyhedral/ball-and-stick representation of the polyanion in **1**. (b) The trilacunary Keggin polyanion {A-SiW_9}. (c) The {A-$P_2Si_2W_{22}$} fragment. (d) The connection diagram of the {Ni_{12}} core and four {PO_4}. (e) The belt-like {P_2W_4} unit. (f) The {Ni_{12}} core. (g) The {$Ni_4(OH)_3$(A-α-SiW_9O_{34})} unit. (h) View of the {Ni_3O_4} quasi-cubane structure. Color legend: WO_6, red octahedra; Ni^{II}, green balls; NiO_6, green octahedra; SiO_4, yellow tetrahedron; PO_4, purple tetrahedron.

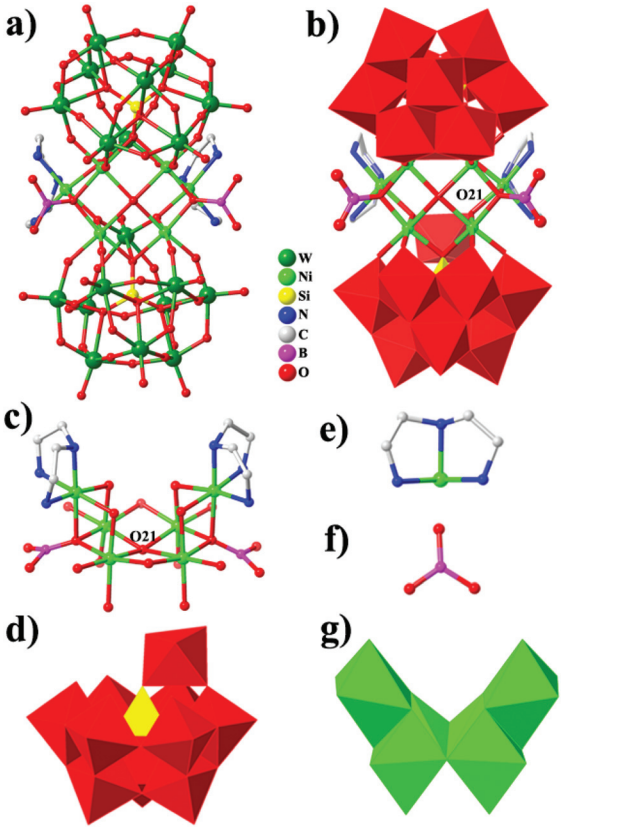

Fig. 2 (a) Ball-and-stick representation of **2**. (b) Combined polyhedral/ball-and-stick representation of compound **2**. (c) The {Ni_6} cluster. (d) The dilacunary Keggin polyanion {B-SiW_{10}}. (e) Coordination view of the Ni atom with dien. (f) The {BO_3} group. (g) The {Ni_6} polyhedron.

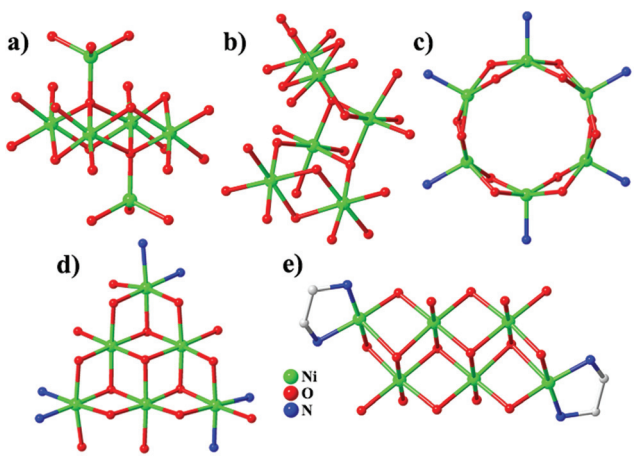

Fig. 3 (a) cross-type {Ni_6} cluster. (b) S type {Ni_6} cluster. (c) hexagonal ring {Ni_6} cluster cluster. (d) plane triangle {Ni_6} cluster. (e) Z type {Ni_6} cluster.

atoms are in the -1 valence state (Table S5, ESI†). Although Gd$(NO_3)_3$ does not crystallize in the structure, it may show subtle influence in adjusting the ionic strength or the pH value of the reaction system, which is crucial for the formation of compound **2**. Interestingly, the boat-like {Ni_6} cluster in **2** is different from other previously reported hexa-nuclear nickel cluster in POM chemistry such as cross-type (Fig. 3a),[41] S-shaped (Fig. 3b),[42] hexagonal ring (Fig. 3c),[43] plane triangle (Fig. 3d)[36] and Z type {Ni_6} cluster (Fig. 3e).[44] Therefore, **2** represents an important new member of hexa-nuclear nickel cluster incorporated TMSPs.

3.3 The photocatalytic performance of 1 and 2 in photoreduction of CO_2

The bandgaps (E_g) of **1** and **2** were calculated by UV-vis diffuse reflection measurements and the Tauc plots of $(ahv)^{1/2}$. The E_g values for **1** and **2** were 2.78 eV and 2.57 eV (Fig. S5, ESI†), respectively, suggesting that they are potential semiconductive materials. The photocatalytic activities of **1** and **2** were initially evaluated by a photocatalytic system of visible-light-driven CO_2 reduction with $[Ru(bpy)_3]Cl_2{\cdot}6H_2O$ and triethanolamine (TEOA) as the photosensitizer and the electron donor,

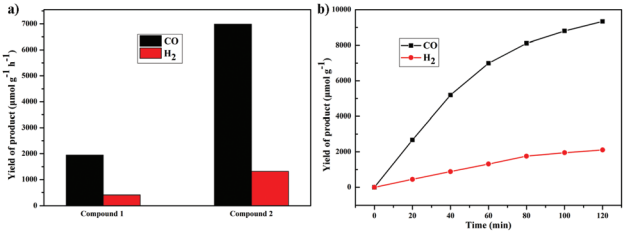

Fig. 4 (a) The yield of CO and H_2 of photoreduction using **1** and **2** as catalysts for 1 h. (b) The effect of the reaction time on the evolution of CO and H_2 from the CO_2 photoreduction. Reaction conditions: compounds (0.1 μmol), $[Ru(bpy)_3]Cl_2{\cdot}6H_2O$ (0.01 mmol) TEOA (1 mL), H_2O (1 mL) and acetonitrile (MeCN, 4 mL).The reaction setup was alternately vacuum degassed and purged with CO_2 three times, after which high-purity CO_2 was purged again for 30 min, $\lambda \geq 420$ nm, 30 °C, 1 h.

respectively.[45–47] The gas products of CO and H_2 were monitored by gas chromatography. Under continuously visible light irradiation, the production of CO and H_2 for **1** and **2** increased as time went by. The yields of CO and H_2 for **1** within 1 h irradiation were 1950 and 410 μmol g^{-1} (TON = 23.71), respectively (Fig. 4a). Different from **1**, the yields of CO and H_2 for **2** within the same time reached to 6988 and 1315 μmol g^{-1} (TON = 83.03), respectively, indicating that **2** is more active than **1** in photocatalytic reduction of CO_2 (Fig. 4a). Hence, the photocatalytic performance of **2** was further studied in detail in this work. As shown in Fig. 4b, the yield of CO increased at a constant speed in the first 40 min, but leveled off after 60 min.

The subsequent drop in performance may be due to the partial decomposition of $[Ru(bpy)_3]Cl_2{\cdot}6H_2O$. To illuminate the origin of CO, an isotope tracer experiment involving $^{13}CO_2$ was carried out. The peaks at 2.7 min and the signal at m/z = 29 were assigned to ^{13}CO, demonstrating that CO originates from CO_2 reduction (Fig. S7, ESI†).

In order to further understand the role of components in photocatalytic system, a series of control experiments were performed (Table S6, ESI†). When the reactions were carried out in dark or nitrogen conditions, there was no CO or H_2 generated. When the experiments were conducted in the absence of photosensitizer or electron donor, the production was negligible, implying that $[Ru(bpy)_3]Cl_2{\cdot}6H_2O$, TEOA are all indispensable for the reaction system. Without **2** as a catalyst, only a trace amount of CO and H_2 were detected, indicating that **2** plays an important role in photoreduction system. In addition, when $Ni(Ac)_2{\cdot}4H_2O$ was used to replace **2** as a catalyst, there was no H_2 produced and only a few CO was detected (TON = 8.02). Meanwhile, the photoreduction activity of the other reaction starting materials, such as $Na_{10}[A\text{-}\alpha\text{-}SiW_9O_{34}]$, were also explored, and there were only negligible CO/H_2 detected. UV-vis spectrum of **2** (1.7×10^{-5} M) was recorded in the solution with different aging time (0–10 h). The UV-vis curves of **2** remain unchanged during the aging course (Fig. S8, ESI†), which indicates the stability of **2** during the process of CO_2 photoreduction. The proposed mechanism of **2** in the photoreduction of CO_2 is presented in Fig. S9, ESI.† The $[Ru(bpy)_3]^{2+}$ is excited from the ground state to the excited state under the irradiation of visible light, and then, it interacts with TEOA to form the reductive photosensitizer. The reductive photosensitizer reverts to the ground state after transferring electrons to **2**. The process can effectively restrain the recombination of the electron–hole pair. Afterward, **2** provides active sites for CO_2 reduction. Ultimately, CO and H_2 are released from the system.[25,27,45]

3.4 Magnetic properties

Variable-temperature magnetic susceptibilities of **1** and **2** were measured between 1.99 and 300 K with an applied magnetic field of 1000 Oe. As shown in Fig. 5, the $\chi_m T$ value of **1** at 300 K is 16.89 cm^3 K mol^{-1}. The value is slightly higher than the theoretical value of 12 cm^3 K mol^{-1} for twelve spin-only Ni^{2+} ions (S = 1 and g = 2.0), which is attributed to the strong orbital contribution of the high-spin octahedral Ni^{2+}. The $\chi_m T$ value declined gradually with the decreasing temperature and reached to a minimum of 12.91 cm^3 K mol^{-1} at 45 K. Below 45 K, the $\chi_m T$ *versus* T curve increased quickly to reach to a maximum of 16.04 cm^3 K mol^{-1} at about 6.44 K and then rapidly dropped to 14.84 cm^3 K mol^{-1} at 1.99 K. The decrease of $\chi_m T$ value from room temperature might be associated with the characteristic spin–orbit coupling of the single Ni^{2+}. Upon further cooling, the sharp upturn of $\chi_m T$ reveals the presence of ferromagnetic interactions within the $\{Ni_{12}\}$ spin core. Finally, the decrease of $\chi_m T$ below 6.44 K is probably ascribed to the existence of magnetic anisotropy of Ni^{2+} ions (zero-field splitting of the ground state) or weak intramolecular antiferromagnetic interactions.[48–50] Although possessing a simple Heisenberg model, it also impossible to model the susceptibility due to the presence of different intramolecular magnetic interactions of the compound and the low symmetry of the Ni_{12} center.[51] Hence, it indicates that antiferromagnetic interactions should be in competition with ferromagnetic ones within the cores.

As shown in Fig. 6, the $\chi_m T$ value of **2** at 300 K is 13.61 cm^3 K mol^{-1}. This value is also slightly higher than the theoretical value of 12 cm^3 K mol^{-1} for twelve spin-only Ni^{II} ions (S = 1 and g = 2.0), which originated from the strong orbital contri-

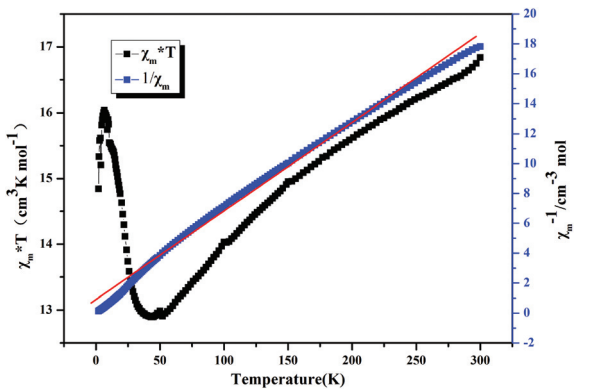

Fig. 5 The temperature dependence of $\chi_m T$ for **1** between 1.99 to 300 K.

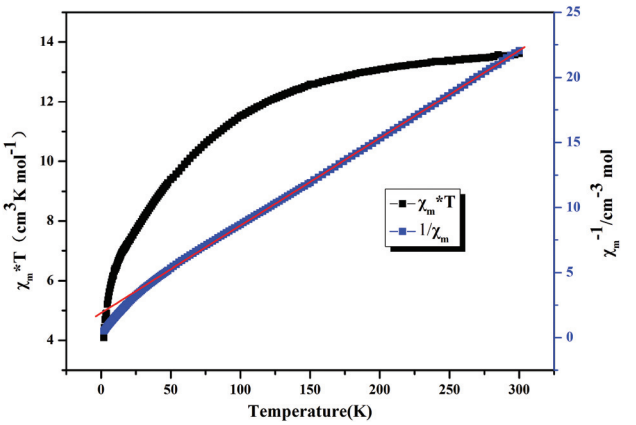

Fig. 6 The temperature dependence of $\chi_m T$ for **2** between 1.99 to 300 K.

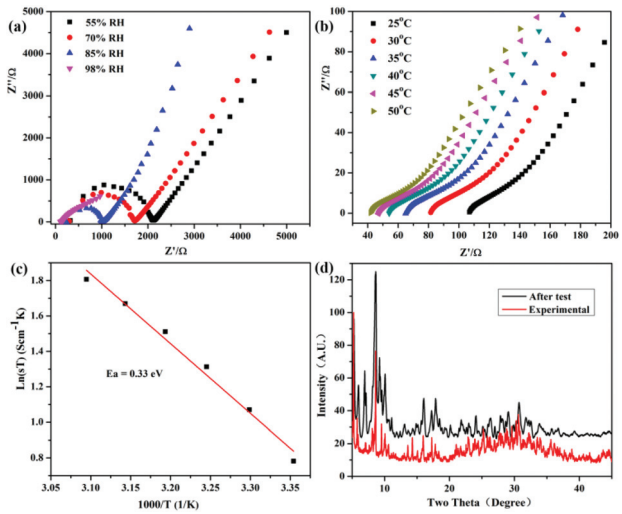

Fig. 7 (a) Nyquist plots for **1** at different RHs and T = 25 °C. (b) Nyquist plots for **1** at different temperatures and 98% RH. (c) Arrhenius plots of the conductivity of **1**. (d) The PXRD patterns of the as-synthesized sample and the sample after proton conductivity test for **1**.

bution of the high-spin octahedral Ni^{2+}. Upon further cooling, the $\chi_m T$ product displayed a sustaining decrease smoothly from 300 K to a minimum of 4.09 cm^3 K mol^{-1} at 1.99 K. This phenomenon shows that there are definitely antiferromagnetic interactions between the Ni^{2+} ions in **2**. Furthermore, alternating current magnetic susceptibilities of **1** and **2** with frequencies between 111 and 2311 Hz were collected under H_{AC} = 3 Oe, and no frequency dependance was observed (Fig. S10 and S11, ESI†).

3.5 Proton conduction study

The presence of large amounts of Na^+, delocalized H^+, and H_2O molecules within **1** prompts us to evaluate its proton conduction performance. Firstly, the relative humidity (RH) dependence on **1** was measured in the range of 55–98% RH at 25 °C. As shown in Fig. 7a, the conductivity (σ) increased from 3.74×10^{-4} S cm^{-1} to 7.33×10^{-3} S cm^{-1} when the RH increased from 55% to 98%, indicating the entry of more water into the structure as mobile proton transfer sites under high humidity conditions.[52,53] Meanwhile, the temperature-dependence conduction behavior of **1** was tested between 25 and 50 °C under 98% RH (Fig. 7b). The Nyquist plots reveal that the conductivity value shows a continuous increase and reaches to the maximum value of 1.89×10^{-2} S cm^{-1} at 98% RH as the temperature rises to 50 °C, indicating that the temperature is more effective than RH in promoting the conductivity. The enhancement of the conductivity as the temperature rises should be attributed to the accelerated transfer of protons in the channel as the temperature increases. The conductivity of **1** at 50 °C under 98% RH is comparable to some reported POM-based proton conductive materials.[54–56] Finally, according to Arrhenius fomula ($\sigma T = \sigma_0 \exp(-E_a/k_b T)$, the activation energy of 0.33 eV was estimated by linear regression analysis, indicating that it belongs to the Grotthuss mechanism (<0.4 eV) (Fig. 7c).[57] The PXRD characterization confirms that the structure of **1** remains intact after proton conductivity experiments (Fig. 7d).

4. Conclusions

In summary, two novel nickel cluster substituted POMs have been successfully synthesized and fully characterized. Interestingly, **1** is a novel Ni_{12}-substituted POM, in which a brand-new {A-$P_2Si_2W_{22}$} fragment is found for the first time. And **2** is an uncommon sandwich-type TMSP structure with a boat-like Ni_6 core. CO_2 photoreduction experiments reveal that **2** exhibits a moderate catalytic activity. Moreover, the proton conduction experiments suggest that **1** may be a potential proton conduction material. This work not only enriches the structural diversity of nickel cluster substituted POM materials, but also extends the applications of TM cluster substituted POMs.

Conflicts of interest

The authors declare no conflicts of interest.

Acknowledgements

This work is financially supported by the National Natural Science Foundation of China (No. 21671040, 21773029 and 21831001), and the Natural Science Foundation of Fujian Provice (No. 2020J01438).

References

1 M. T. Pope and A. Miiller, Polyoxometalate Chemistry: An Old Field with New Dimensions in Several Disciplines, *Angew. Chem., Int. Ed. Engl.*, 1991, **30**, 34–48.

2 C. L. Hill, Introduction: Polyoxometalates-Multicomponent Molecular Vehicles To Probe Fundamental Issues and Practical Problems, *Chem. Rev.*, 1998, **98**, 1–2.
3 P. Kögerler and L. Cronin, Polyoxometalate Nanostructures, Superclusters, and Colloids: From Functional Clusters to Chemical Aesthetics, *Angew. Chem., Int. Ed.*, 2005, **44**, 844–846.
4 D. L. Long, E. Burkholder and L. Cronin, Polyoxometalate clusters, nanostructures and materials: From self assembly to designer materials and devices, *Chem. Soc. Rev.*, 2007, **36**, 105–121.
5 S. S. Mal and U. Kortz, The Wheel–Shaped Cu_{20} Tungstophosphate $[Cu_{20}Cl(OH)_{24}(H_2O)_{12}(P_8W_{48}O_{184})]^{25-}$ Ion, *Angew. Chem., Int. Ed.*, 2005, **44**, 3777–3780.
6 B. S. Bassil, M. H. Dickman, I. Römer, B. V. D. Kammer and U. Kortz, The Tungstogermanate $[Ce_{20}Ge_{10}W_{100}O_{376}(OH)_4(H_2O)_{30}]^{56-}$: A Polyoxometalate Containing 20 Cerium(III) Atoms, *Angew. Chem., Int. Ed.*, 2007, **46**, 6192–6195.
7 M. Ibrahim, V. Mereacre, N. Leblanc, W. Wernsdorfer, C. E. Anson and A. K. Powell, Self-Assembly of a Giant Tetrahedral 3d-4f Single-Molecule Magnet within a Polyoxometalate System, *Angew. Chem., Int. Ed.*, 2015, **54**, 15574–15578.
8 S. Reinoso, M. Giménez-Marqués, J. R. Galán-Mascarós, P. Vitoria and J. M. Gutiérrez-Zorrilla, Giant Crown-Shaped Polytungstate Formed by Self-Assembly of CeIII-Stabilized Dilacunary Keggin Fragments, *Angew. Chem., Int. Ed.*, 2010, **49**, 8384–8388.
9 X. X. Li, Y. X. Wang, R. H. Wang, C. Y. Cui, C. B. Tian and G. Y. Yang, Designed Assembly of Heterometallic Cluster Organic Frameworks Based on Anderson-Type Polyoxometalate Clusters, *Angew. Chem., Int. Ed.*, 2016, **55**, 6462–6466.
10 W. W. Guo, H. J. Lv, K. P. Sullivan, W. O. Gordon, A. Balboa, G. W. Wagner, D. G. Musaev, J. Bacsa and C. L. Hill, Broad-Spectrum Liquid- and Gas-Phase Decontamination of Chemical Warfare Agents by One-Dimensional Heteropolyniobates, *Angew. Chem., Int. Ed.*, 2016, **55**, 7403–7407.
11 K. Ichihashi, D. Konno, K. Y. Maryunina, K. Inoue, K. Toyoda, S. Kawaguchi, Y. Kubota, Y. Tatewaki, T. Akutagawa, T. Nakamura and S. Nishihara, Selective Ion Exchange in Supramolecular Channels in the Crystalline State, *Angew. Chem., Int. Ed.*, 2019, **58**, 4169–4172.
12 L. J. Chen, D. Y. Shi, J. W. Zhao, Y. L. Wang, P. T. Ma, J. P. Wang and J. Y. Niu, Three Transition-Metal Substituted Polyoxotungstates Containing Keggin Fragments: From Trimer to One-Dimensional Chain to Two-Dimensional Sheet, *Cryst. Growth Des.*, 2011, **11**, 1913–1923.
13 L. Huang, S. S. Wang, J. W. Zhao, L. Cheng and G. Y. Yang, Synergistic Combination of Multi-Zr^{IV} Cations and Lacunary Keggin Germanotungstates Leading to a Gigantic Zr_{24}-Cluster-Substituted Polyoxometalate, *J. Am. Chem. Soc.*, 2014, **136**, 7637–7642.
14 V. Singh, Z. Y. Chen, P. T. Ma, D. D. Zhang, M. G. B. Drew, J. Y. Niu and J. P. Wang, Unprecedented $\{Fe_{14}\}/\{Fe_{10}\}$ Polyoxotungstate-Based Nanoclusters with Efficient Photocatalytic H_2 Evolution Activity: Synthesis, Structure, Magnetism, and Electrochemistry, *Chem. – Eur. J.*, 2016, **22**, 10983–10989.
15 L. Huang, J. Zhang, L. Cheng and G. Y. Yang, Poly(polyoxometalate)s assembled by $\{Ni_6PW_9\}$ units: from ring-shaped Ni_{24}-tetramers to rod-shaped Ni_{40}-octamers, *Chem. Commun.*, 2012, **48**, 9658–9660.
16 S. T. Zheng and G. Y. Yang, Recent advances in paramagnetic-TM-substituted polyoxometalates (TM = Mn, Fe, Co, Ni, Cu), *Chem. Soc. Rev.*, 2012, **41**, 7623–7646.
17 H. M. Zhang, Y. G. Li, Y. Lu, R. Clérac, Z. M. Zhang, Q. Wu, X. J. Feng and E. B. Wang, Sandwich-Type Phosphotungstates: Structure, Electrochemistry, and Magnetism of the Trinickel-Substituted Polyoxoanion $[Ni_3Na(H_2O)_2(PW_9O_{34})_2]^{11-}$, *Inorg. Chem.*, 2002, **41**, 6412–6416.
18 I. M. Mbomekalle, B. Keita, M. Nierlich, U. Kortz, P. Berthet and L. Nadjo, Structure, Magnetism, and Electrochemistry of the Multinickel Polyoxoanions $[Ni_6As_3W_{24}O_{94}(H_2O)_2]^{17-}$, $[Ni_3Na(H_2O)_2(AsW_9O_{34})_2]^{11-}$, and $[Ni_4Mn_2P_3W_{24}O_{94}(H_2O)_2]^{17-}$, *Inorg. Chem.*, 2003, **42**, 5143.
19 P. Mialane, A. Dolbecq, E. Rivière, J. Marrot and F. Sécheresse, A Polyoxometalate Containing the $\{Ni_2N_3\}$ Fragment: Ferromagnetic Coupling in a Ni^{II} μ-1,1 Azido Complex with a Large Bridging Angle, *Angew. Chem., Int. Ed.*, 2004, **43**, 2274–2277.
20 X. M. Luo, L. Chen, Y. Y. Dong, J. Li, C. H. Cui, J. P. Cao and Y. Xu, Three new high-nuclear transition-metal substituted heteropolytungstates: syntheses, crystal structures, magnetic studies and NLO properties, *Dalton Trans.*, 2018, **47**, 9504–9511.
21 Z. W. Cai, T. Yang, Y. J. Qi, X. X. Li and S. T. Zheng, A temperature-resolved assembly of a series of the largest scandium-containing polyoxotungstates, *Dalton Trans.*, 2017, **46**, 6848–6852.
22 V. A. Ghisolfi, K. Y. Monakhov, R. Pattacini, P. Braunstein, X. López, C. d. Graaf, M. Speldrich, J. v. Leusen, H. Schilder and P. Kögerler, A comparative synthetic, magnetic and theoretical study of functional M_4Cl_4 cubane-type Co(II) and Ni(II) complexes, *Dalton Trans.*, 2014, **43**, 7847–7859.
23 S. T. Zheng, J. Zhang, J. M. Clemente-Juan, D. Q. Yuan and G. Y. Yang, Poly(polyoxotungstate)s with 20 Nickel Centers: From Nanoclusters to One-Dimensional Chains, *Angew. Chem., Int. Ed.*, 2009, **48**, 7176–7179.
24 H. H. Lv, Y. N. Chi, J. V. Leusen, P. Kçgerler, Z. Y. Chen, J. Bacsa, Y. V. Geletii, W. W. Guo, T. Q. Lian and C. L. Hill, $[\{Ni_4(OH)_3AsO_4\}_4(B\text{-}\alpha\text{-}PW_9O_{34})_4]^{28-}$: A New Polyoxometalate Structural Family with Catalytic Hydrogen Evolution Activity, *Chem. – Eur. J.*, 2015, **21**, 17363–17370.
25 X. B. Han, Y. G. Li, Z. M. Zhang, H. Q. Tan, Y. Lu and E. B. Wang, Polyoxometalate-Based Nickel Clusters as

Visible Light-Driven Water Oxidation Catalysts, *J. Am. Chem. Soc.*, 2015, **137**, 5486–5493.

26 X. J. Kong, Z. K. Lin, Z. M. Zhang, T. Zhang and W. B. Lin, Hierarchical Integration of Photosensitizing Metal-Organic Frameworks and Nickel-Containing Polyoxometalates for Efficient Visible-Light-Driven Hydrogen Evolution, *Angew. Chem., Int. Ed.*, 2016, **55**, 6411–6416.

27 L. Yu, Y. Ding, M. Zheng, H. L. Chen and J. W. Zhao, $[\{\beta\text{-}SiNi_2W_{10}O_{36}(OH)_2(H_2O)\}_4]^{24-}$: a new robust visible light-driven water oxidation catalyst based on nickel-containing polyoxometalate, *Chem. Commun.*, 2016, **52**, 14494–14497.

28 X. B. Han, C. Qin, X. L. Wang, Y. Z. Tan, X. J. Zhao and E. B. Wang, Bio-inspired assembly of cubane-adjustable polyoxometalate-based high-nuclear nickel clusters for visible light-driven hydrogen evolution, *Appl. Catal., B*, 2017, **211**, 349–356.

29 X. X. Li, D. Zhao and S. T. Zheng, Recent advances in POM-organic frameworks and POM-organic polyhedra, *Coord. Chem. Rev.*, 2019, **397**, 220–240.

30 S. T. Zheng, J. Zhang and G. Y. Yang, Designed Synthesis of POM-Organic Frameworks from $\{Ni_6PW_9\}$ Building Blocks under Hydrothermal Conditions, *Angew. Chem., Int. Ed.*, 2008, **47**, 3909–3913.

31 S. T. Zheng, D. Q. Yuan, H. P. Jia, J. Zhang and G. Y. Yang, Combination between lacunary polyoxometalates and high-nuclear transition metal clusters under hydrothermal conditions: I. from isolated cluster to 1-D chain, *Chem. Commun.*, 2007, 1858–1860.

32 X. X. Li, S. T. Zheng, J. Zhang, W. H. Fang, G. Y. Yang and J. M. Clemente-Juan, High-Nuclearity Ni-Substituted Polyoxometalates: A Series of Poly(polyoxotungstate)s Containing 20–22 Nickel Centers, *Chem. – Eur. J.*, 2011, **17**, 13032–13043.

33 X. X. Li, W. H. Fang, J. W. Zhao and G. Y. Yang, The First 3-Connected $SrSi_2$-Type 3D Chiral Framework Constructed from $\{Ni_6PW_9\}$ Building Units, *Chem. – Eur. J.*, 2015, **21**, 2315–2318.

34 X. X. Li, S. T. Zheng, W. H. Fang and G. Y. Yang, A series of Ni_6-substituted polyoxometalates derivated from tripodal alcohol ligands, *Inorg. Chem. Commun.*, 2011, **14**, 1541–1545.

35 X. X. Li, W. H. Fang and G. Y. Yang, Hydrothermal synthesis and crystal structure of a novel sandwich germanotungstate: $[Ni(dien)(H_2O)_3]_2[Ni(Hdien)_2]\{[Ni(dien)]_2Ni_4(H_2O)_2(GeW_9O_{34})_2\}\cdot 10H_2O$, *Chem. J. Chin. Univ.*, 2011, **32**, 571–576.

36 X. X. Li, W. H. Fang, J. W. Zhao and G. Y. Yang, Hydrothermal Combination of Trilacunary Dawson Phosphotungstates and Hexanickel Clusters: From an Isolated Cluster to a 3D Framework, *Chem. – Eur. J.*, 2014, **20**, 17324–17332.

37 G. Herve and A. Teze, Study of .alpha.- and .beta.-enneatungstosilicates and -germanates, *Inorg. Chem.*, 1977, **16**, 2115–2117.

38 Z. Y. Ma, R. Q. Wang, T. Yu and L. H. Bi, Preparation, characterization and catalytic performance of polyoxometalate immobilized on the surface of halloysite, *J. Mater. Sci.*, 2019, **54**, 3817–3831.

39 H. M. Zhang, Y. G. Li, Y. Lu, R. Clérac, Z. M. Zhang, Q. Wu, X. J. Feng and E. B. Wang, A New Ni_{12} Cluster Based on Polyoxometalate Ligands, *Inorg. Chem.*, 2009, **48**, 10889–10891.

40 S. J. Li, S. X. Liu, Q. Tang, Y. W. Liu, D. F. He, S. T. Wang and Z. Shi, Borate-templated self-assembly of multinuclear nickel(II)-containing POMs, *Dalton Trans.*, 2013, **42**, 13319–13322.

41 J. P. Wang, P. T. Ma, Y. Shen and J. Y. Niu, A Novel Polyoxotungstate $[Ni_4(H_2O)_2(\alpha\text{-}NiW_9O_{34})_2]^{16-}$ Based on an Old Structure with a New Component, *Cryst. Growth Des.*, 2007, **7**, 603–605.

42 Z. M. Zhang, Y. G. Li, E. B. Wang, X. L. Wang, C. Qin and H. Y. An, Synthesis, Characterization, and Crystal Structures of Two Novel High-Nuclear Nickel-Substituted Dimeric Polyoxometalates, *Inorg. Chem.*, 2006, **45**, 4313–4315.

43 Z. F. Zhao, B. B. Zhou, S. T. Zheng, Z. H. Su and C. M. Wang, Hydrothermal synthesis, crystal structure and magnetic characterization of three hexa-M substituted tungstoarsenates (M = Ni, Zn and Mn), *Inorg. Chim. Acta*, 2009, **362**, 5038–5042.

44 W. J. Niu, D. Y. Shi, J. W. Zhao, X. M. Cai and L. J. Chen, An organic–inorganic hybrid hexa-nickel substituted sandwich-type germanotungstate $[enH_2]_2[Ni(en)_2]_2\{[Ni_6(en)_2(H_2O)_2][B\text{-}\alpha\text{-}GeW_9O_{34}]_2\}\cdot 14H_2O$, *Inorg. Chem. Commun.*, 2012, **17**, 79–83.

45 W. Yao, C. Qin, N. Xu, J. Zhou, C. Y. Sun, L. Liu and Z. M. Su, Visible-light CO_2 photoreduction of polyoxometalate-based hybrids with different cobalt clusters, *CrystEngComm*, 2019, **21**, 6423–6431.

46 X. Zhao, J. Zhou, C. Y. Sun, S. Q. You, X. L. Wang and Z. M. Su, A ruthenium/polyoxometalate for efficient CO_2 photoreduction under visible light in diluted CO_2, *Nanotechnology*, 2020, **31**, 255402.

47 Y. Benseghir, Al. Lemarchand, Ma. Duguet, P. Mialane, M. Gomez-Mingot, C. Roch-Marchal, T. Pino, M. Ha-Thi, M. Haouas, M. Fontecave, A. Dolbecq, C. Sassoye and C. Mellot-Draznieks, Co-immobilization of a Rh Catalyst and a Keggin Polyoxometalate in the UiO-67 Zr-Based Metal-Organic Framework: In Depth Structural Characterization and Photocatalytic Properties for CO_2 Reduction, *J. Am. Chem. Soc.*, 2020, **142**, 9428–9438.

48 J. W. Zhao, B. Li, S. T. Zheng and G. Y. Yang, Two-Dimensional Extended (4,4)-Topological Network Constructed from Tetra-Ni^{II}-Substituted Sandwich-Type Keggin Polyoxometalate Building Blocks and Ni^{II}-Organic Cation Bridges, *Cryst. Growth Des.*, 2007, **7**, 2658–2664.

49 P. T. Ma, J. W. Zhao, J. P. Wang, Y. Shen and J. Y. Niu, Sandwich-type polyoxotungstate hybrids decorated by nickel-aromatic amine complexes, *J. Solid State Chem.*, 2010, **183**, 150–156.

50 M. Ibrahim, Y. X. Xiang, B. S. Bassil, Y. H. Lan, A. K. Powell, P. d. Oliveira, B. Keita and U. Kortz, Synthesis,

Magnetism, and Electrochemistry of the Ni_{14}- and Ni_5-Containing Heteropolytungstates $[Ni_{14}(OH)_6(H_2O)_{10}(HPO_4)_4(P_2W_{15}O_{56})_4]^{34-}$ and $[Ni_5(OH)_4(H_2O)_4(\beta\text{-}GeW_9O_{34})(\beta\text{-}GeW_8O_{30}(OH))]^{13-}$, *Inorg. Chem.*, 2013, **52**, 8399–8408.

51 H. M. Zhang, Y. G. Li, Y. Lu, R. Clérac, Z. M. Zhang, Q. Wu, X. J. Feng and E. B. Wang, A New Ni_{12} Cluster Based on Polyoxometalate Ligands, *Inorg. Chem.*, 2009, **48**, 10889–10891.

52 G. J. Cao, J. D. Liu, T. T. Zhuang, X. H. Cai and S. T. Zheng, A polyoxometalate-organic supramolecular nanotube with high chemical stability and proton-conducting properties, *Chem. Commun.*, 2015, **51**, 2048–2051.

53 Z. Li, L. D. Lin, D. Zhao, Y. Q. Sun and S. T. Zheng, A Series of Unprecedented Linear Mixed-Metal-Substituted Polyoxometalate Trimers: Syntheses, Structures, Luminescence, and Proton Conductivity Properties, *Eur. J. Inorg. Chem.*, 2019, **2019**, 437–441.

54 Z. Li, X. X. Li, T. Yang, Z. W. Cai and S. T. Zheng, Four-Shell Polyoxometalates Featuring High-Nuclearity Ln_{26} Clusters: Structural Transformations of Nanoclusters into Frameworks Triggered by Transition-Metal Ions, *Angew. Chem., Int. Ed.*, 2017, **56**, 2664–2669.

55 B. X. Liu, Z. W. Cai, T. Yang, X. X. Li, G. Y. Yang and S. T. Zheng, A Rare Polyoxometalate Based on Mixed Niobium-Based Polyoxoanions $[GeNb_{18}O_{54}]^{14-}$ and $[Nb_3W_3O_{19}]^{5-}$, *Inorg. Chem. Commun.*, 2017, **78**, 56–60.

56 P. Yang, M. Alsufyani, A. H. Emwas, C. Q. Chen and N. M. Khashab, Lewis Acid Guests in a $\{P_8W_{48}\}$ Archetypal Polyoxotungstate Host: Enhanced Proton Conductivity via Metal-Oxo Cluster within Cluster Assemblies, *Angew. Chem., Int. Ed.*, 2018, **57**, 13046–13051.

57 A. Shigematsu, T. Yamada and H. Kitagawa, Wide Control of Proton Conductivity in Porous Coordination Polymers, *J. Am. Chem. Soc.*, 2011, **133**, 2034–2036.